Research Article | Vol. 31, No. 11 / 22 May 2023 / Optics Express 18177
Optics EXPRESS

# White-light channeled imaging polarimeter using Savart plates and a polarization Sagnac interferometer

JUN CHEN,[1,2,3] XIAOTIAN LI,[1,2,3,*] JIRI JIRIGALANTU,[1,3] FUGUAN LI,[1,2,3] QIHANG CHU,[1,2,3] YUQI SUN,[1,2,3] AND HESHIG BAYAN[1,2,3]

[1] *Changchun Institute of Optics, Fine Mechanics and Physics, Chinese Academy of Sciences, Changchun Jilin 130033, China*
[2] *University of Chinese Academy of Sciences, Beijing 100049, China*
[3] *National Engineering Research Center for Diffraction Gratings Manufacturing and Application, Changchun Jilin 130033, China*
[*] *lixiaotian@ciomp.ac.cn*

**Abstract:** A Stokes white-light channeled imaging polarimeter using Savart plates and a polarization Sagnac interferometer (IPSPPSI) is presented, which provides an effective solution to the problem of channel aliasing in broadband polarimeters. The expression for the light intensity distribution and a method to reconstruct polarization information are derived, and an example design for an IPSPPSI is given. The results reveal that a complete measurement of the Stokes parameters in broad band can be achieved with a snapshot on a single detector. The use of dispersive elements like gratings suppresses broadband carrier frequency dispersion so the channels in the frequency domain do not affect each other, ensuring the integrity of information coupled across the channels. Furthermore, the IPSPPSI has a compact structure and does not employ moving parts or require image registration. It shows great application potential in remote sensing, biological detection, and other fields.



## 1. Introduction

Traditional imaging techniques use cameras to measure light intensity incident on photosensitive surfaces to record information about the color and shape of the imaged object. Polarization imaging technology can record not only the intensity but also the polarization of the optical fields, including the degree of polarization [1], the polarization angle [2], the polarization ellipticity [3], and so on, which significantly increase the amount of information. The polarization state of electromagnetic waves can be described by the four Stokes parameters. Many areas like space exploration [4], biomedicine [5,6], and environmental testing [7,8] require the instantaneous acquisition of the Stokes parameters.

Stokes imaging polarimeters can identify either the partial or complete polarization state of an object by determining the Stokes parameters. To completely characterize the Stokes parameters requires sequentially recording light intensity from the target with at least four different polarized states, for example by using a rotating retarder, a linear polarizer, an imaging lens, and a detector [9,10]. Such time-sequential measurements are compatible with traditional spectrometers, but there are moving elements in the optical path, which lead to poor system stability and an inability to measure moving objects or scenes containing motion. There are also time-sequential polarimeters without moving parts, which change the polarization states of light by applying devices such as liquid-crystal variable retarders [11,12] or piezoelectric retarders [13], and so on. However, these polarimeters still cannot acquire multiple polarization parameters at once and

#487423 https://doi.org/10.1364/OE.487423
Journal © 2023 Received 10 Feb 2023; revised 13 Apr 2023; accepted 19 Apr 2023; published 15 May 2023

have a weak ability for dynamic measurements. In many applications, the measure of polarization parameters is obtained from moving platforms [14,15].

To measure moving targets, the apparatus must acquire multiple light intensities in parallel. Instruments based on division of focal plane [16,17], division of amplitude [18–21], division of aperture [22–24], and channeled imaging polarimeters [25–27] can obtain all or several Stokes parameters within a single measurement (a snapshot). The channeled imaging polarimeter has an intrinsic advantage compared with other listed polarimeters because it possesses inherent image registration: the Stokes vectors are spatially dependent and modulated onto various interferometrically generated carrier frequencies [28].

The method of encoding Stokes parameters onto spatial carrier frequencies was proposed by K. Oka [29], who established a complete Stokes imaging polarimeter [30] through the use of optimized Wollaston prisms. On the basis of channeled modulated polarization imaging technology, different polarization interference imaging polarimeters have been designed using Savart plates [31], polarization Sagnac interferometers [32], polarization gratings [33], and so on. However, imaging polarimeters with Savart plates are only suitable for operation in quasi-monochromatic light conditions because of carrier frequency dispersion. The narrow bandwidth limits the application range of these polarimeters and often adversely affects the signal-to-noise ratio. Michael W. Kudenov achieved polarization imaging over the white light range (400-700 nm) by using gratings to compensate dispersion for the carrier frequency, but he only measured partial Stokes parameters of the target in a snapshot [28].

In this paper, we present the theoretical development of a new type of channeled modulated snapshot polarimeter working across the white light range, which we call the Imaging Polarimeter using Savart Plates and Polarization Sagnac Interferometer (IPSPPSI). The IPSPPSI is capable of acquiring the complete, two-dimensional distribution of the Stokes polarization parameters in broadband. In addition, the instrument possesses a simple and compact structure, high stability, and low cost. This paper describes the principles of the IPSPPSI in detail and provides a theoretical design. The polarimeter is numerically simulated in the range from 400 nm to 700 nm, and finally, the simulation results are presented.

## 2. System model

The basic configuration of the IPSPPSI is depicted in Fig. 1. The IPSPPSI consists of Savart plates (SP), a wire-grated polarizing beam splitter (WGBS), two reflective blazed gratings (G1 and G2 in Fig. 1), a linear polarizer (LP), an imaging lens, and a CCD camera. The proposed polarization imager generates a spatial shear parallel to the y-axis through the Savart plates and a shear parallel to the x-axis using the Sagnac interference structure (comprising WGBS, G1, and G2). The Savart plates comprise two uniaxial crystals of the same thickness, which are rotated 45° clockwise around the z-axis, as shown in Fig. 2(a). The optic axes (indicated by the blue dashed line in Fig. 2(a)) of the two Savart plates are located in the ABCD plane and the ADEF plane, respectively, and at an angle of 45 degrees with the z-axis. The two mirrors of the classic Sagnac interference structure are replaced with gratings G1 and G2, which are angled 67.5° from the x-axis and the z-axis, respectively. G1 and G2 are the same distance from the WGBS. The usual orientation of the WGBS is at a 45° angle to the x- and z-axes. The linear polarizer is perpendicular to the direction of light transmission, and its polarization direction is 45°. The CCD camera is placed in the focal plane of the imaging lens.

A geometric ray model was used to explore the system's principles. The incident light undergoes lateral shear after transmission through the SP, splitting into two orthogonally polarized beams. Because the SP rotates 45° around the z-axis, the polarization directions of the two beams also change, with each beam polarizing at 45° with respect to the x- and y-axes, as illustrated in

Optics EXPRESS

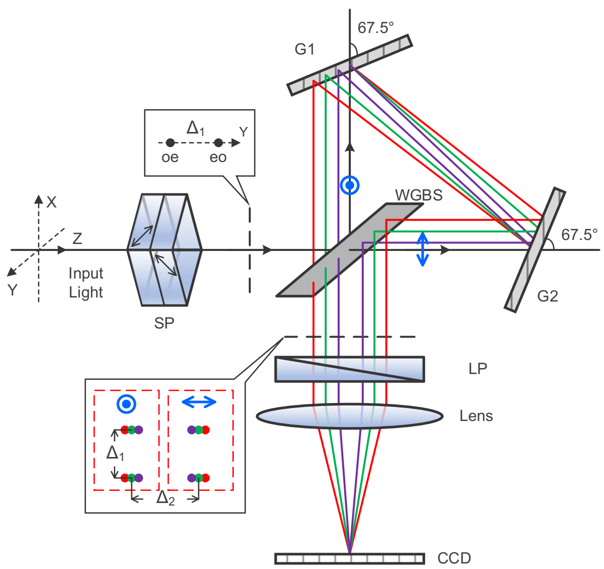


**Fig. 1.** Optical layout of an IPSPPSI with ray tracing at three representative wavelengths. "oe" and "eo" denote two possible changes in polarization through the Savart plates (SP): "oe" indicates a change from ordinary (o) to extraordinary (e) light, and "eo" indicates the reverse. $\Delta_1$ and $\Delta_2$ represent the shearing distances caused by the Savart plates and the polarization Sagnac interferometer, respectively.

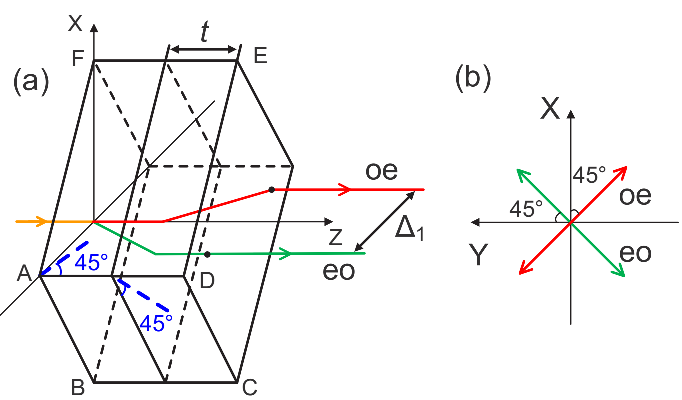


**Fig. 2.** (a) Schematic of the Savart plates (SP), including arrows that indicate the light propagation direction. (b) The polarization directions of the output light from the SP.

Optics EXPRESS

Fig. 2(b). The shear distance $\Delta_1$ produced by the SP is [34]:

$$\Delta_1 = \sqrt{2}\frac{n_o^2 - n_e^2}{n_o^2 + n_e^2}t \tag{1}$$

where $n_e$ and $n_o$ are the extraordinary and ordinary refractive indices of the SP, respectively. $t$ represents the thickness of a single Savart plate. Because the SP are birefringent, a geometric optical path difference ($OPD_{sp}$) is created between the ordinary and extraordinary rays, which can be expressed as [35]:

$$OPD_{sp} = \sqrt{2}t\frac{n_o^2 - n_e^2}{n_o^2 + n_e^2}\cos\omega\sin\alpha \tag{2}$$

where $\omega$ denotes the angle between the plane of incidence and the principal section of the Savart plates, and $\alpha$ is the incident angle. Normally $\omega = 0$, so Eq. (2) can be simplified to:

$$OPD_{sp} = \Delta_1 \sin\alpha \tag{3}$$

Similar to the SP, the WGBS divides the light into two linearly polarized beams perpendicular to each other, with one transmitted and the other reflected.

G1 and G2 are identical blazed diffraction gratings. It is well known that:

$$d(\sin i - \sin\theta) = m\lambda \tag{4}$$

where $d$ is the period of G1 and G2, $i$ is the incident angle, $\theta$ is the diffraction angle, $m$ is the diffraction order, and λ is the wavelength. Light is spatially modulated by the polarization Sagnac interference structure (i.e. WGBS, G1, and G2), producing a shear displacement $\Delta_2$ perpendicular to the SP. Assuming the diffraction angle is small, then $\Delta_2$ has the form [28]:

$$\Delta_2 = \frac{2m\lambda a}{d} \tag{5}$$

where $a$ denotes the distance between G1 and G2. Therefore, under certain conditions, the shear $\Delta_2$ generated by the polarization Sagnac interferometer is proportional to the wavelength. The optical path difference ($OPD_{Sag}$) produced by the polarization Sagnac interferometer is similar to that of the SP. It can be written as follows:

$$OPD_{Sag} = \Delta_2 \sin\beta \tag{6}$$

where $\beta$ is the incidence angle. The input light undergoes spatial modulation in different orientations after passing through the SP, the WGBS, and G1 and G2, splitting from one beam into four. The polarizations of these rays become parallel after passing the linear polarizer. Finally, the rays are imaged on the CCD camera using the lens to obtain an interference fringe image.

The Stokes parameters can be defined by the following formulae:

$$\begin{aligned} S_0 &= \langle E_x E_x^* \rangle + \langle E_y E_y^* \rangle \\ S_1 &= \langle E_x E_x^* \rangle - \langle E_y E_y^* \rangle \\ S_2 &= \langle E_x E_y^* \rangle + \langle E_x^* E_y \rangle \\ S_3 &= j\left(\langle E_x E_y^* \rangle - \langle E_x^* E_y \rangle\right) \end{aligned} \tag{7}$$

where < > indicates the time average and * signifies conjugate calculations. The two-dimensional distribution of the Stokes parameters of the input image is defined as $S_0(x, y)$, $S_1(x, y)$, $S_2(x, y)$, and $S_3(x, y)$, where x, y are spatial coordinates in the scene. Then the light intensity distribution acquired by the CCD camera is:

$$\begin{aligned} I(x,y) = {} & \frac{1}{2}S_0(x,y) + \frac{1}{2}S_1(x,y)\cos(\varphi_2-\varphi_1) \\ & + \frac{1}{4}S_2(x,y)\cos(\varphi_3-\varphi_1) + \frac{1}{4}S_3(x,y)\sin(\varphi_3-\varphi_1) \\ & - \frac{1}{4}S_2(x,y)\cos(\varphi_4-\varphi_2) - \frac{1}{4}S_3(x,y)\sin(\varphi_4-\varphi_2) \end{aligned} \tag{8}$$

where $\varphi_1$, $\varphi_2$, $\varphi_3$, $\varphi_4$ are the cumulative phases of each ray. Under ideal conditions, $\varphi_1$ through $\varphi_4$ can be written as [36]:

$$\begin{aligned} \varphi_1 &= -\tfrac{2\pi}{\lambda f}\tfrac{\Delta_2 x}{2}, \varphi_2 = \tfrac{2\pi}{\lambda f}\tfrac{\Delta_2 x}{2} \\ \varphi_3 &= \tfrac{2\pi}{\lambda f}(\tfrac{\Delta_2 x}{2}+\Delta_1 y), \varphi_4 = \tfrac{2\pi}{\lambda f}(-\tfrac{\Delta_2 x}{2}+\Delta_1 y) \end{aligned} \tag{9}$$

where $f$ is the focal length of the imaging lens. Replacing the phase factors $\varphi_1$ to $\varphi_4$ in Eq. (8) with these expressions produces:

$$\begin{aligned} I(x,y) = {} & \frac{1}{2}S_0(x,y) + \frac{1}{2}S_1(x,y)\cos(2\pi U_2 x) \\ & + \frac{1}{4}S_2(x,y)\cos[2\pi(U_2 x + U_1 y)] + \frac{1}{4}S_3(x,y)\sin[2\pi(U_2 x + U_1 y)] \\ & - \frac{1}{4}S_2(x,y)\cos[2\pi(U_2 x - U_1 y)] + \frac{1}{4}S_3(x,y)\sin[2\pi(U_2 x - U_1 y)] \end{aligned} \tag{10}$$

The spatial carrier frequencies (frequencies of the interference fringes) represented by $U_1$ and $U_2$ in Eq. (10) are related to the SP and the polarization Sagnac interferometer, respectively. $U_1$ and $U_2$ are:

$$\begin{aligned} U_1 &= \tfrac{\Delta_1}{\lambda f} = \tfrac{\sqrt{2}t(n_o^2-n_e^2)}{\lambda f(n_o^2+n_e^2)} \\ U_2 &= \tfrac{\Delta_2}{\lambda f} = \tfrac{2ma}{df} \end{aligned} \tag{11}$$

Aside from the wavelength λ, the structural parameters of the IPSPPSI can be regarded as constants. Consequently, $U_1$ changes when the input wavelengths change, while $U_2$ is invariant within the spectral range 400-700 nm.

As illustrated in Eq. (10), $S_0$ is a DC term unaffected by the carrier frequencies; $S_1(x, y)$ implicitly depends on x, while $S_2$ and $S_3$ are spatially modulated by $U_1$ and $U_2$ simultaneously. Hence, the Stokes parameters except $S_0$ are amplitude-modulated onto several carrier frequencies. As a result, Fourier filtering can be applied to decouple the polarization information in the frequency domain and obtain different channels that contain the Stokes vectors. By taking an inverse Fourier transform of the filtered carrier frequencies, or "channels," it is possible to demodulate the polarization information and extract the Stokes parameters [37]. Performing a Fourier transform on the interference pattern I(x, y) yields:

$$\begin{aligned} \mathcal{F}[I(x,y)] = {} & \tfrac{S_0(x,y)}{2} * \delta(f_x,f_y) + \tfrac{1}{4}S_1(x,y) * [\delta(f_x+U_2,f_y) + \delta(f_x-U_2,f_y)] \\ & + \tfrac{1}{8}[S_2(x,y) + jS_3(x,y)] * \delta(f_x+U_2,f_y+U_1) \\ & + \tfrac{1}{8}[S_2(x,y) - jS_3(x,y)] * \delta(f_x-U_2,f_y-U_1) \\ & - \tfrac{1}{8}[S_2(x,y) - jS_3(x,y)] * \delta(f_x+U_2,f_y-U_1) \\ & - \tfrac{1}{8}[S_2(x,y) + jS_3(x,y)] * \delta(f_x-U_2,f_y+U_1) \end{aligned} \tag{12}$$

where $\delta$ donates the Dirac delta function, and $f_x$ and $f_y$ are the angular spectral components of x and y, respectively.

Optics EXPRESS

According to Eq. (12), there are seven channels in the Fourier domain. Their distribution is shown in Fig. 3, where red boxes indicate the channels required to demodulate the polarization parameters. The $S_2$ and $S_3$ Stokes vectors are convolved by two shifted delta functions ($U_1$ and $U_2$), and the $S_1$ parameter is influenced by the delta function of $U_2$, while $S_0$ is unmodulated. Inverse Fourier transformation of channels $C_0$, $C_1$, and $C_2$ yields:

$$\mathcal{F}^{-1}(C_0) = \frac{1}{2}S_0(x, y) \tag{13}$$

$$\mathcal{F}^{-1}(C_1) = \frac{1}{4}S_1(x, y)\exp(j2\pi U_2) \tag{14}$$

$$\mathcal{F}^{-1}(C_2) = -\frac{1}{8}(S_2(x, y) + jS_3(x, y))\exp(-j2\pi U_1)\exp(j2\pi U_2) \tag{15}$$

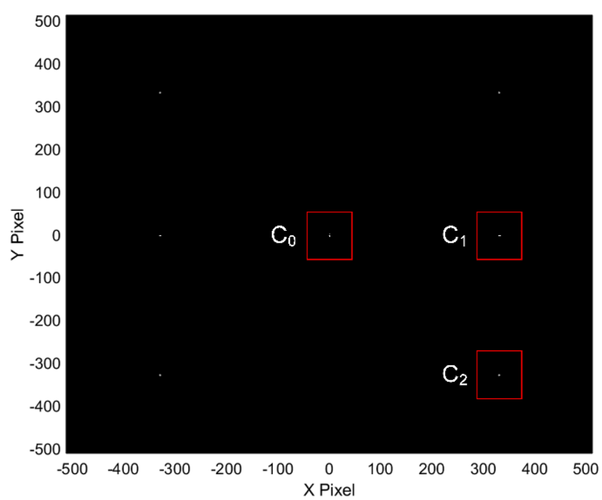


**Fig. 3.** The two-dimensional interference pattern when the incident light is monochromatic (550 nm). Channels $C_0$-$C_2$ are labeled and indicated by red squares. The diffraction order is considered to be 1; the grating separation *a* is 35 mm; the imaging lens focal length *f* is 100 mm; the pixel size is 13 µm, and the dimensions of the sensor are 1024 × 1024 pixels.

According to Eq. (13), $S_0$ can be obtained directly by Fourier transforming twice. The exponential phase factors exp(-$j2\pi U_1$) and exp($j2\pi U_2$) interfere with the extraction of $S_1$, $S_2$, and $S_3$. However, these phase factors are determined by the polarimeter parameters but independent of the incident beams, so they can be decoupled using reference beam calibration. It is appropriate in most cases to demodulate the Stokes parameters using a uniformly polarized image formed by a linear polarizer oriented at 22.5° as the Ref. [38].

The complete Stokes vectors contained in the channels can be calculated using reference light demodulation technology, and the unknown sample data are recovered as follows:

$$S_{0,reference,22.5^\circ}(x, y) = |\mathcal{F}(C_{0,reference,22.5^\circ})| \tag{16}$$

$$S_{0,sample}(x, y) = |\mathcal{F}(C_{0,sample})| \tag{17}$$

$$S_{1,sample}(x, y) = \Re\left[\frac{\mathcal{F}(C_{1,sample})}{\mathcal{F}(C_{1,reference,22.5^\circ})}\frac{S_{0,reference,22.5^\circ}}{S_{0,sample}}\right] \tag{18}$$

$$S_{2,sample}(x, y) = \Re\left[\frac{\mathcal{F}(C_{2,sample})}{\mathcal{F}(C_{2,reference,22.5^\circ})}\frac{S_{0,reference,22.5^\circ}}{S_{0,sample}}\right] \tag{19}$$

$$S_{3,sample}(x,y) = \Im\left[\frac{\mathcal{F}(C_{2,sample})}{\mathcal{F}(C_{2,reference,22.5^\circ})}\frac{S_{0,reference,22.5^\circ}}{S_{0,sample}}\right] \tag{20}$$

where $\Re$ and $\Im$ represent the real and imaginary parts of the expression.

## 3. Method of reconstruction

Previous applications of the polarization Sagnac interferometer to polarization imaging polarimeters in the white light range have been reported [39], but they can only obtain partial Stokes parameters of the target in a single snapshot. Complete polarization information about the target can be measured by including two Savart plates [40], but because of the limitations of the operating principle—the carrier frequency of the SP varies with wavelength, resulting in channel aliasing in frequency domain and decreased interference fringe visibility—can work well only when light is quasi-monochromatic. The interference fringe period is the reciprocal of the carrier frequency:

$$T_k = \frac{1}{U_k}, k = 1 \text{ or } 2. \tag{21}$$

In the IPSPPSI, the carrier frequencies along the x- and y-axes of the CCD are inconsistent, resulting in different interference fringe periods in the two directions. Note that the SP consists of birefringent crystals (like calcite), and according to Eq. (11), the refractive indices of ordinary and extraordinary light are related to the spatial carrier frequency $U_1$, which may affect the value of $T_1$. The refractive indices of ordinary and extraordinary light in a birefringent crystal are calculated by (also taking calcite as an example) [41]:

$$n_o^2 = 1.73358749 + \frac{0.96464345\lambda^2}{\lambda^2 - 1.94325203/100} + \frac{1.82831454\lambda^2}{\lambda^2 - 120} \tag{22}$$

$$n_e^2 = 1.35859695 + \frac{0.82427830\lambda^2}{\lambda^2 - 1.06689543/100} + \frac{0.14429128\lambda^2}{\lambda^2 - 120}. \tag{23}$$

When $\lambda$ varies from 400 nm to 700 nm, the fluctuation amplitude of $n_o$ is 1.76% and that of $n_e$ is 0.90%, so it is reasonable to ignore the effect of the refractive index on the fringe periods. Therefore, $T_1$ is not fixed because $U_1$ varies with the wavelength of a broadband light source, while $T_2$ remains almost constant.

Simulated images of the white-light interference fringes and the channels in the interferogram are shown in Fig. 4. Figure 4(a) and Fig. 4(b) are consistent with Eq. (21). Because of the broad bandwidth, the profile along the y-axis of the polarization interference image (Fig. 4(b)) has that there is no obvious periodicity. Figure 4(c) and Fig. 4(d) show the frequency domain distribution. $C_0$ is at zero frequency without being affected by the change in carrier frequency, but in order to better observe the effect of broadband imaging on the remaining channels, the DC component has been removed. The channels can still be clearly distinguished in white light. Compared with the data in Fig. 3, the position of each channel on the x-axis has not changed, but $S_2$ and $S_3$ extend into lines along the y-axis. Matching the SP's thickness and grating constants ensures the integrity of the information contained in each channel, thus ensuring the high-precision reconstruction of the Stokes parameters.

Optics EXPRESS

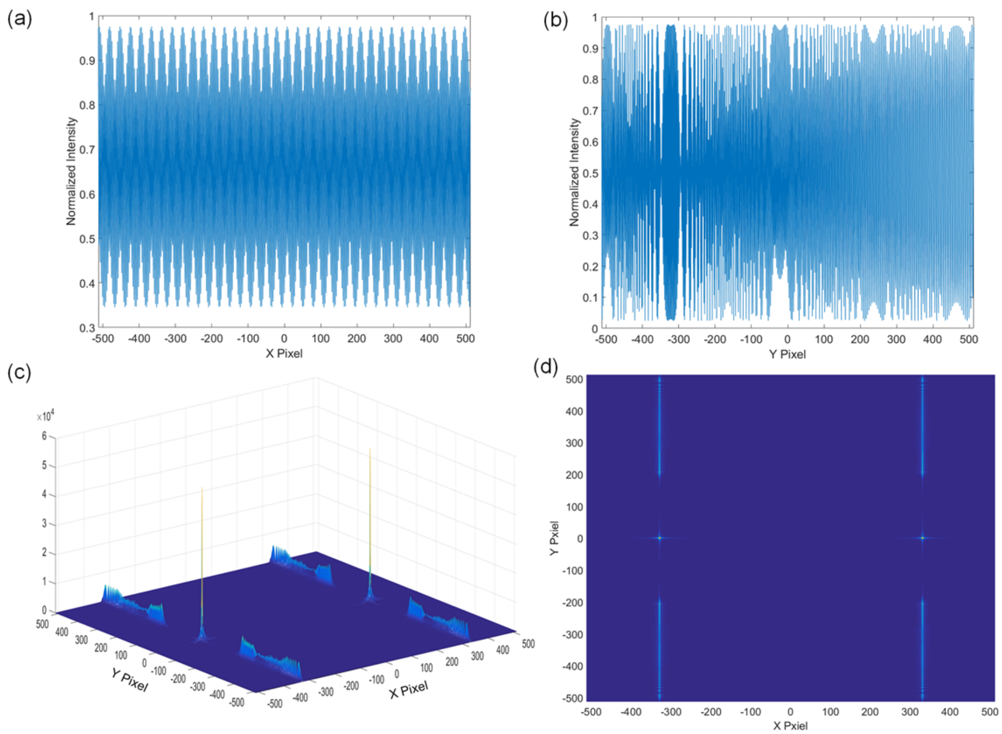


**Fig. 4.** Simulation results for the white-light interference image profile and its angular spectrum. (a) The image section at 0 of the x axis in the focal plane. (b) The image section at 0 of the y axis in the focal plane. (c) Fourier spectra of the 2D interference pattern produced by the IPSPPSI. (d) Top view of (c).

## 4. Numerical simulation

To more intuitively demonstrate the advantages of the imaging polarimeter described in this paper, specific structural parameters were chosen to simulate the model. The simulation is based on the following parameters: $t = 5$ mm, $n_o = 1.6613$, $n_e = 1.4875$, $d = 28$ μm, and $f = 100$ mm; the pixel size is 13 μm, and the CCD pixel array is $1024 \times 1024$. The reference data used for calibration come from a uniformly polarized image formed by a linear polarizer at 22.5°, with standard Stokes values of $S_1 = 0.707$, $S_2 = 0.707$, and $S_3 = 0$. An image corresponding to a uniformly polarized picture in white light with different polarization states was simulated. Figure 5 depicts the variation of carrier frequencies along the x and y axes as a function of wavelength. The positions of the seven channels on the x axis in the frequency domain do not change because $U_2$ is constant. The reconstructed Stokes and reference data are presented in Fig. 6. The RMS deviations of the reconstructed values of $S_0$, $S_1$, $S_2$, and $S_3$ from the input values were calculated for each pixel and summarized in Table 1; the parameter with the largest deviation is $S_2$. The reference and reconstructed data values are very close, with only 0.0126 mean RMS error.

**Table 1. The RMS error between the reconstructed and the theoretical value of normalized Stokes parameters for a uniformly polarized picture**

| Stokes parameter | $S_0$ | $S_1$ | $S_2$ | $S_3$ |
|---|---|---|---|---|
| RMS error | 0.0091 | 0.0043 | 0.0223 | 0.0145 |
| Mean | | 0.0126 | | |

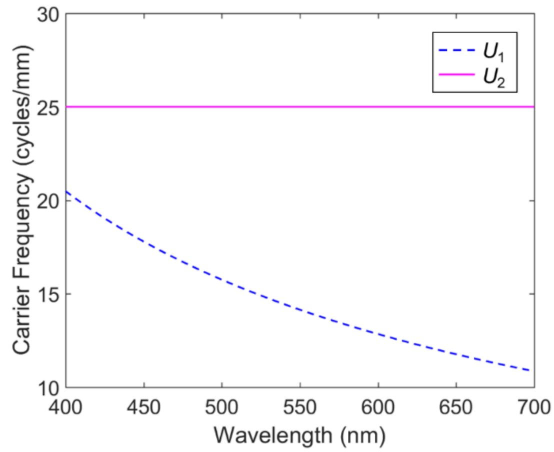


**Fig. 5.** The carrier frequencies $U_1$ (blue dashed line) and $U_2$ (pink line) as a function of wavelength along their respective axes.

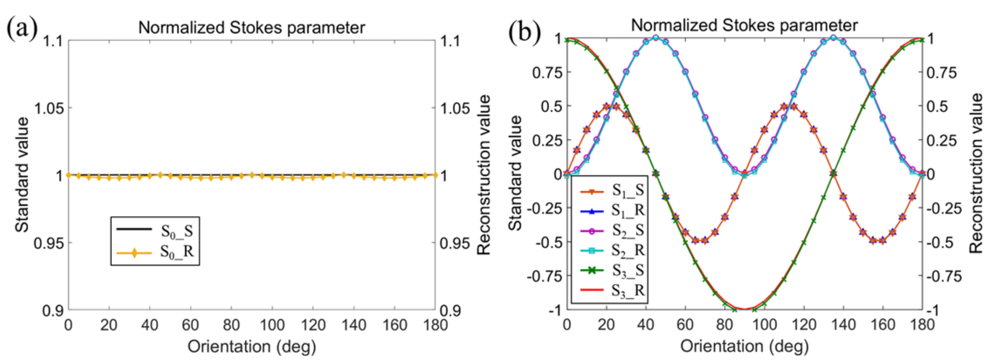


**Fig. 6.** Comparison between the reconstructed Stokes parameters and standard values when a 45° linear polarizer and a quarter-wave plate that rotates between 0° and 180° are added in the front of the IPSPPSI to simulate different polarization states. (a) The theoretical values of $S_0$ ($S_0$_S, black curve) and the reconstruction values of $S_0$ ($S_0$_R, yellow curve). (b) The theoretical and the reconstruction values of $S_1$ (red and blue triangles), $S_2$ (magenta circle and cyan square), and $S_3$ (green bow and red line), where _S and _R are defined as above.

Optics EXPRESS

Next, the ideal Stokes object depicted in Fig. 7(a) was used as input. The object simultaneously contains different polarization states. The simulated polarization interference pattern that results when the IPSPPSI modulates the input is shown in Fig. 7(b). Figure 8 shows the images of $S_0$, $S_1$, $S_2$, and $S_3$ reconstructed from the polarization interference pattern. A two-dimensional rectangular filter was used to extract the desired channels and minimize the impact of adjacent ones. However, some high-frequency information is lost while adjacent channels' high spatial frequencies are retained; these are difficult to decouple because they are obscured by lower spatial frequencies. Nevertheless, the IPSPPSI retains high accuracy, as shown in Table 2: the mean RMS error is 0.0223.

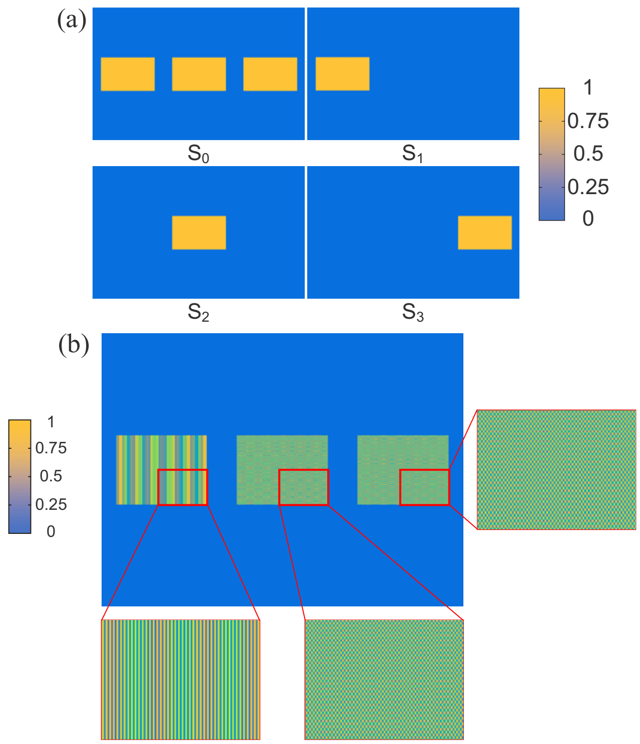


**Fig. 7.** (a) The ideal Stokes object; (b) The polarization interference pattern through the IPSPPSI.

**Table 2. The RMS error between the reconstructed and the theoretical value of normalized Stokes parameters for a picture contains different polarization states**

| Stokes parameter | $S_0$ | $S_1$ | $S_2$ | $S_3$ |
|---|---|---|---|---|
| RMS error | 0.0297 | 0.0043 | 0.0277 | 0.0275 |
| Mean | | 0.0223 | | |

The most important optical elements of the IPSPPSI are the Savart plates and gratings, whose structural parameters directly affect the shearing distance and, in turn, the extraction and reconstruction of polarization information. Figure 9 explores the influence of changes in the grating period and the thickness of the Savart plates on the position of channel $C_2$ in the frequency domain. Figure 9(a) illustrates how the grating period affects $C_2$'s x-axis coordinates. The position of $C_2$ is very sensitive to grating fabrication error when the grating constant is small, and a slight change in $d$ can cause a drastic change in position. If $C_2$ is located near pixel 0

Optics EXPRESS

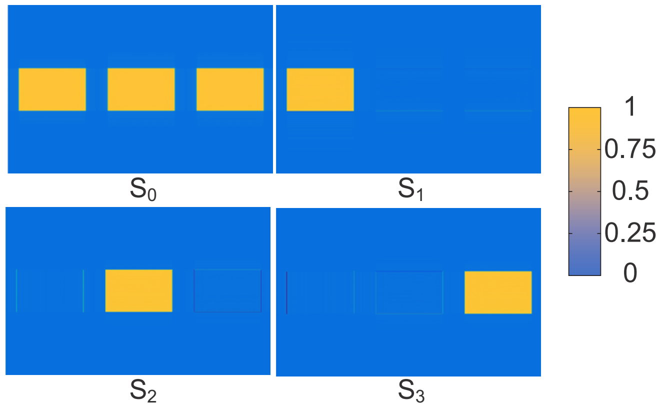


**Fig. 8.** The reconstructed Stokes parameters.

or 512, it will be difficult to extract the polarization information completely, which will affect the reconstruction results. To ensure the accuracy of the reconstructed Stokes parameters, the grating groove density should not be too large, and the channel should be centered. For example, gratings with a period greater than 5μm and the x-axis position in Fig. 9(a) from 100 to 400 are more conducive to data processing. Figure 9(b) shows the y-axis dispersion of broadband light between 400 and 700 nm as a function of the thickness of the Savart plates. When t is in the range from 9.389 mm to 17.714 mm, polarization information from the target cannot be completely extracted because of the periodicity of the Fourier transform in the limited space, and the error on the reconstructed Stokes parameters is large. The corresponding part of the range in the figure is blank because it is not considered suitable for the viable range of t. As t increases, the 400 nm and 700 nm boundaries switch position. The principle to follow when selecting the SP thickness is that the channel boundaries (the locations of 400 nm or 700 nm in Fig. 9(b)) cannot be too close to 0. For instance, we suggest channel boundaries be less than -15.

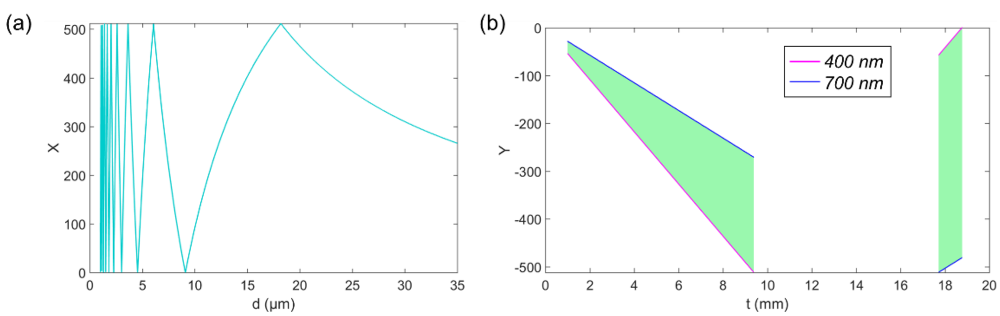


**Fig. 9.** (a) Effect of the grating period on the x-axis position of channel $C_2$ in the frequency domain. (b) The relationship between the y-axis position of channel $C_2$ at wavelengths between 400 and 700 nm and the thickness of a single Savart plate. For frequency domain space, the center is set to 0, and x and y range from -512 to 512.

## 5. Conclusion

This work presents a compact design for a snapshot polarization interferometric imaging polarimeter, the IPSPPSI. The IPSPPSI contains a Savart plate and a polarization Sagnac interferometer. The polarization characteristics of the SP and interferometer are analyzed in detail, and a theoretical design is provided. Unlike traditional polarization interference imaging polarimeters, the IPSPPSI can completely characterize the Stokes parameters within a broadband snapshot. Its blazed gratings effectively suppress carrier frequency dispersion under broadband conditions and ensure the independence of the channels so the coupled polarization data will not affect each other, which maintains high precision in the reconstructed data.

An example of an IPSPPSI is provided. Simulations show that the proposed polarimeter can separate the polarization information carried by the target in the frequency domain. The use of gratings makes the position of each channel along the x axis of the frequency domain wavelength-independent, suppressing the channel aliasing over the visible spectrum. The distribution of channels can be determined using the parameters of the SP and gratings. For objects with either uniformly polarization or complex polarization states, the reconstructed Stokes parameters retain high accuracy.

In addition, the influence of the grating period and SP thickness on the channel distribution are analyzed. The grating period can be selected within a wide range, but it should not be too small, in order to avoid large effects from grating fabrication errors. The thickness of the SP also needs to fall within a specific range.

Finally, the IPSPPSI has the advantages of a compact structure, no moving parts, and no need for image registration. We expect that the IPSPPSI will have great application potential in many fields, such as space exploration, biomedicine, environmental testing, and remote sensing.

**Funding.** National Natural Science Foundation of China (52227810, 61975255, U2006209); Jilin Province Research Projects in China (20230401091YY).

**Acknowledgments.** We thank Kaley McCluskey, PhD, for English grammar assistance.

**Disclosures.** The authors declare that they have no known competing financial interests or personal relationships that could have appeared to influence the work reported in this paper.

**Data availability.** No data generated or analyzed in the presented research.

## References

1. J. E. Solomon, "Polarization imaging," Appl. Opt. **20**(9), 1537–1544 (1981).
2. V. Gruev, R. Perkins, and T. York, "CCD polarization imaging sensor with aluminum nanowire optical filters," Opt. Express **18**(18), 19087–19094 (2010).
3. C. Chen-Kuan, C. Wei-Liang, F. Peter Tramyeon, L. Sung-Jan, L. Hsuan-Shu, and D. Chen-Yuan, "Polarization ellipticity compensation in polarization second-harmonic generation microscopy without specimen rotation," J. Biomed. Opt. **13**(1), 014005 (2008).
4. G. Chin, S. Brylow, M. Foote, J. Garvin, J. Kasper, J. Keller, M. Litvak, I. Mitrofanov, D. Paige, K. Raney, M. Robinson, A. Sanin, D. Smith, H. Spence, P. Spudis, S. Stern, and M. Zuber, "Lunar Reconnaissance Orbiter Overview: The Instrument Suite and Mission," Space Sci. Rev. **129**(4), 391–419 (2007).
5. A. Sanaz and I. A. Vitkin, "Polarized light imaging in biomedicine: emerging Mueller matrix methodologies for bulk tissue assessment," J. Biomed. Opt. **20**(6), 061104 (2015).
6. T. York, S. B. Powell, S. Gao, L. Kahan, T. Charanya, D. Saha, N. W. Roberts, T. W. Cronin, J. Marshall, S. Achilefu, S. P. Lake, B. Raman, and V. Gruev, "Bioinspired Polarization Imaging Sensors: From Circuits and Optics to Signal Processing Algorithms and Biomedical Applications," Proc. IEEE **102**(10), 1450–1469 (2014).
7. M. Yang, W. Xu, Z. Sun, H. Wu, Y. Tian, and L. Li, "Mid-wave infrared polarization imaging system for detecting moving scene," Opt. Lett. **45**(20), 5884–5887 (2020).
8. S. Leigh, Z. Wang, and D. A. Clausi, "Automated Ice–Water Classification Using Dual Polarization SAR Satellite Imagery," IEEE Trans. Geosci. Remote Sensing **52**(9), 5529–5539 (2014).
9. H. G. Berry, G. Gabrielse, and A. E. Livingston, "Measurement of the Stokes parameters of light," Appl. Opt. **16**(12), 3200–3205 (1977).
10. B. Schaefer, E. Collett, R. Smyth, D. Barrett, and B. Fraher, "Measuring the Stokes polarization parameters," American Journal of Physics - AMER J PHYS 75, (2007).
11. J. Bailey, L. Kedziora-Chudczer, D. Cotton, K. Bott, J. Hough, and P. Lucas, "A high-sensitivity polarimeter using a ferro-electric liquid crystal modulator," Mon. Not. R. Astron. Soc. **449**(3), 3064–3073 (2015).
12. G. Myhre, W.-L. Hsu, A. Peinado, C. Lacasse, N. Brock, R. Chipman, and S. Pau, "Liquid crystal polymer full-stokes division of focal plane polarimeter," Opt. Express **20**(25), 27393–27409 (2012).
13. M. Ginya, Y. Mizutani, T. Iwata, and Y. Otani, "Polarization properties of PLZT under applied voltage measured by dual-rotating retarder polarimeter," Phys. Procedia **19**, 398–402 (2011).

Optics EXPRESS


14. N. Quan, C. Zhang, T. Yan, Q. Li, R. Gao, and T. Mu, "Linear stokes imaging spectropolarimeter based on the static polarization interference imaging spectrometer," Opt. Commun. **391**, 30–36 (2017).
15. W. K. Michael, J. L. Pezzaniti, and R. G. Grant, "Microbolometer-infrared imaging Stokes polarimeter," Opt. Eng. **48**(6), 063201 (2009).
16. R. Perkins and V. Gruev, "Signal-to-noise analysis of Stokes parameters in division of focal plane polarimeters," Opt. Express **18**(25), 25815–25824 (2010).
17. T. Mu, S. Pacheco, Z. Chen, C. Zhang, and R. Liang, "Snapshot linear-Stokes imaging spectropolarimeter using division-of-focal-plane polarimetry and integral field spectroscopy," Sci. Rep. **7**(1), 42115 (2017).
18. O. Morel, R. Seulin, and D. Fofi, "Handy method to calibrate division-of-amplitude polarimeters for the first three Stokes parameters," Opt. Express **24**(12), 13634–13646 (2016).
19. X. Tu, O. J. Spires, X. Tian, N. Brock, R. Liang, and S. Pau, "Division of amplitude RGB full-Stokes camera using micro-polarizer arrays," Opt. Express **25**(26), 33160–33175 (2017).
20. R. M. A. Azzam, "Division-of-amplitude Photopolarimeter (DOAP) for the Simultaneous Measurement of All Four Stokes Parameters of Light," Optica Acta: International Journal of Optics **29**(5), 685–689 (1982).
21. N. Christian, L. Zheng, L. Thomas, and B. Jürgen, "Simplified Stokes polarimeter based on division-of-amplitude," Proc. SPIE **11144**, 111441B (2019).
22. J. S. Tyo, "Hybrid division of aperture/division of a focal-plane polarimeter for real-time polarization imagery without an instantaneous field-of-view error," Opt. Lett. **31**(20), 2984–2986 (2006).
23. W. Zhang, J. Liang, L. Ren, H. Ju, E. Qu, Z. Bai, Y. Tang, and Z. Wu, "Real-time image haze removal using an aperture-division polarimetric camera," Appl. Opt. **56**(4), 942–947 (2017).
24. T. Mu, C. Zhang, and R. Liang, "Demonstration of a snapshot full-Stokes division-of-aperture imaging polarimeter using Wollaston prism array," J. Opt. **17**(12), 125708 (2015).
25. M. W. Kudenov, M. J. Escuti, E. L. Dereniak, and K. Oka, "White-light channeled imaging polarimeter using broadband polarization gratings," Appl. Opt. **50**(15), 2283–2293 (2011).
26. J. L. Dennis, F. L. I. V. Charles, and M. C. Julia, "Compressed channeled linear imaging polarimetry," Proc. SPIE **10407**, 104070D (2017).
27. J. L. Dennis, "Compressive sensing for channeled polarimetry: applications in spectropolarimetry and imaging polarimetry," Proc. SPIE **11130**, 111300D (2019).
28. M. W. Kudenov, M. E. L. Jungwirth, E. L. Dereniak, and G. R. Gerhart, "White light Sagnac interferometer for snapshot linear polarimetric imaging," Opt. Express **17**(25), 22520–22534 (2009).
29. O. Yoshihiro and O. Kazuhiko, "Polarimeter for mapping spatial distribution of dynamic state of polarization," in Proc. SPIE (1992), pp. 42–48.
30. K. Oka and T. Kaneko, "Compact complete imaging polarimeter using birefringent wedge prisms," Opt. Express **11**(13), 1510–1519 (2003).
31. O. Kazuhiko and S. Naooki, "Snapshot complete imaging polarimeter using Savart plates," Proc. SPIE **6295**, 629508 (2006).
32. A. W. Abdallah and M. Abdelwahab, "A modified method for calibration of polarimetric components using polarizing interferometry," Meas. Sci. Technol. **32**(11), 115003 (2021).
33. M. W. Kudenov, M. J. Escuti, N. Hagen, E. L. Dereniak, and K. Oka, "Snapshot imaging Mueller matrix polarimeter using polarization gratings," Opt. Lett. **37**(8), 1367–1369 (2012).
34. J. Geake, "Polarization interferometers: applications in microscopy and macroscopy by M. Francon and S. Mallick," J. Appl. Crystallogr. **5**(5), 387 (1972).
35. Q. Cao, C. Zhang, and E. DeHoog, "Snapshot imaging polarimeter using modified Savart polariscopes," Appl. Opt. **51**(24), 5791–5796 (2012).
36. H. Luo, K. Oka, E. DeHoog, M. Kudenov, J. Schiewgerling, and E. L. Dereniak, "Compact and miniature snapshot imaging polarimeter," Appl. Opt. **47**(24), 4413–4417 (2008).
37. A. Taniguchi, K. Oka, H. Okabe, and M. Hayakawa, "Stabilization of a channeled spectropolarimeter by self-calibration," Opt. Lett. **31**(22), 3279–3281 (2006).
38. M. W. Kudenov, N. A. Hagen, E. L. Dereniak, and G. R. Gerhart, "Fourier transform channeled spectropolarimetry in the MWIR," Opt. Express **15**(20), 12792–12805 (2007).
39. S. Jin, J. Xing, P. Hu, M. Hu, and G. Xia, "Polarization Sagnac interferometer with reflective grating for white-light channeled imaging polarimeter," Opt. Laser Technol. **108**, 529–533 (2018).
40. H. Luo, "Snapshot imaging polarimeters using spatial modulation," (2008).
41. G. Ghosh, "Dispersion-equation coefficients for the refractive index and birefringence of calcite and quartz crystals," Opt. Commun. **163**(1-3), 95–102 (1999).